Pulse compression by a refractive index front in periodically modulated silicon waveguide

Boyi Zhang [1], Maurice Pfeiffer [1], Mahmoud A. Gaafar [1,2,3], He Li [4], Xinlun Cai [4], Juntao Li [4,*], Manfred Eich [1,5], and Alexander Yu. Petrov [1,5,†]

[1] *Institute of Optical and Electronic Materials, Hamburg University of Technology, Hamburg 21073, Germany*

[2] *Department of Physics, Faculty of Science, Menoufia University, Menoufia, Egypt*

[3] *Directed Energy Research Centre, Technology Innovation Institute, Abu Dhabi SE45-01, United Arab Emirates*

[4] *State Key Laboratory of Optoelectronic Materials & Technology, Sun Yat-sen University, Guangzhou 510275, China*

[5] *Institute of Functional Materials for Sustainability, Helmholtz-Zentrum Hereon, Max-Planck-Strasse 1, Geesthacht D-21502, Germany*

(Received 18 February 2025; accepted 21 November 2025; published 12 January 2026)

In this study, we report the experimental demonstration of optical pulse compression with a gradual refractive index front comoving in a periodically modulated silicon waveguide. This spatiotemporal effect, also called optical push broom, captures and confines the input signal pulse inside a faster propagating refractive index front, driven by a pump pulse. The signal is accelerated by the approaching front until its velocity matches the front's velocity, effectively stopping the light relative to the front. In contrast with the previous experiment where we used a cw signal, we now utilized a pulsed signal and thus can vary the initial delay between the signal and the pump. We employ the slowly varying envelope approximation to model the effect and successfully reproduce the experimental frequency shift at the output corresponding to the temporal delay at the input.

DOI: 10.1103/6x6w-p51w

I. INTRODUCTION

Interest in light interactions with time-varying media is growing due to their capability for manipulation of not only the wave number but also the frequency of light [1–3]. In waveguide and photonic crystal systems, additional flexibility is added by the possibility to design dispersion [4–8]. Specifically, moving fronts represent a particular type of spatiotemporal perturbations [9–19] that can lead to significant changes in the frequency and wave number of the signal light. Dispersion plays a fundamental role in defining the final state of light [9]. Particular interest is presented by the waveguides with periodic perturbation where the fast front captures and compresses slow light pulses, offering a promising approach for one-step pulse compression [10–13]. It can be shown that the interaction with the index front can be generally considered as an indirect transition of the signal state, altering its frequency and wave number [14,15]. Depending on the dispersion of the waveguide before and after the front and the direction of the indirect transition, the signal is shifted to the perturbed states, behind the front, or back to the original states, before the front, which results in the transmission or reflection from the front (see Fig. 1) [9,16–20]. The reflection case also includes the so-called optical event horizon effects [21,22]. However, if the transition goes parallel in between perturbed and original dispersion relations, the trapping of the pulse is realized as signal does not find states before and after the front and is bound to stay inside it [9]. The front captures and accelerates the signal pulse up to the front speed and compresses it. The transition is not complete, whereas the frequency and wave number of the signal are continuously changing as it propagates in the front. The trapping case also includes the optical push broom effect [23]. This trapping effect shares conceptual similarities with the light localization in tapered plasmonic waveguides, where the surface-plasmon polariton stops in the taper without reflection [12,24].

De Sterke first predicted that the energy of a weak probe could be made to heap up on the pump's leading edge propagating in a fiber Bragg grating using nonlinear coupled-mode equations for forward and backward propagating waves [23]. Later, the Schrödinger equation description was given to describe the optical push broom effect involving cross-phase modulation in highly dispersive media [25]. Recently, Gaafar *et al.* demonstrated the analytical solutions for pulse compression in a linear front [12] where a perturbed dispersion relation is piecewise linear and is shifted in frequency with respect to the original dispersion relation. In this case, finite compression of the signal is achieved by the Fourier transform of the input signal, which resembles focusing by a lens. On the other hand, Pendry presented an analytical model to describe the compression of signal pulses interacting with a refractive index front that leads to the change of the slope of the dispersion relation [13]. In this case, compression in the front is continuous and might lead to singularities. Yet, experimental progress has lagged behind theoretical developments. Broderick *et al.* reported the attempt to realize the optical push broom

*Contact author: lijt3@mail.sysu.edu.cn

†Contact author: a.petrov@tuhh.de

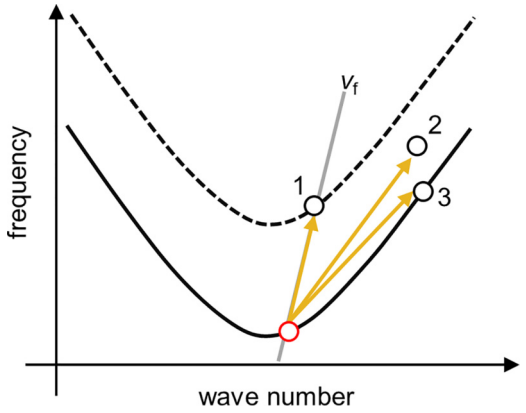

FIG. 1. Schematic of the front-induced indirect transitions with different front velocity v_f, which determines the direction of the transition [9]. The solid curve represents the dispersion of the original mode, while the dashed one represents the dispersion of the mode perturbed by the index front. The red circle represents the initial state, and the black circles 1, 2, 3 represent the final states of signal light in the case of transmission, trapping, and reflection, respectively. The gray straight line represents the phase continuity line with the slope determined by v_f (only shows for case 1 for clarity). The yellow arrows show the direction of indirect transitions for different v_f.

in fiber Bragg gratings by the Kerr effect [10]. They showed that a small portion of a cw signal could be cut out and concentrated inside the index front. Since then, many pioneering works have studied the dynamic pulse control in integrated photonics, particularly the cross-phase modulation [26–28] and slow light effects [29–35]. We have previously shown the trapping effect in periodically modulated silicon waveguides using free carrier excitation as the front and cw signal [36]. Also, different systems are utilized now to generate strong fronts in epsilon near-zero media, but propagation lengths stay very short due to intrinsic absorption of such media [37,38].

In this study, we achieved the first experimental confirmation of the optical push broom effect in a silicon Bragg waveguide, demonstrated through a pump-probe experiment by varying the delay between pump and probe. We took advantage of the strong silicon waveguide's nonlinearity by free carrier dispersion [39] and customizable dispersion of the periodic silicon waveguide [40–42]. The induced refractive index change is much smaller than in epsilon near-zero media [43], but much larger propagation distances are possible. A slowly varying envelope approximation is employed to model the signal pulse propagation. The free carrier front is generated via two-photon absorption of a 2 ps pump pulse centered at a frequency below the band gap of the Bragg waveguide. The 10 ps signal pulse is tuned close to the upper band edge and propagates initially slower than the pump. Our experimental results show that the signal pulse is collected by the front and converted into new frequencies, with an estimated temporal compression of up to 2.5 times. One step further, the delay-dependent measurements untangle the Fourier transformation performed by the front [12]. We show that the temporal delay at the input results in the frequency shift at the output, which is predicted by the analytical model and well reproduced by numerical simulations.

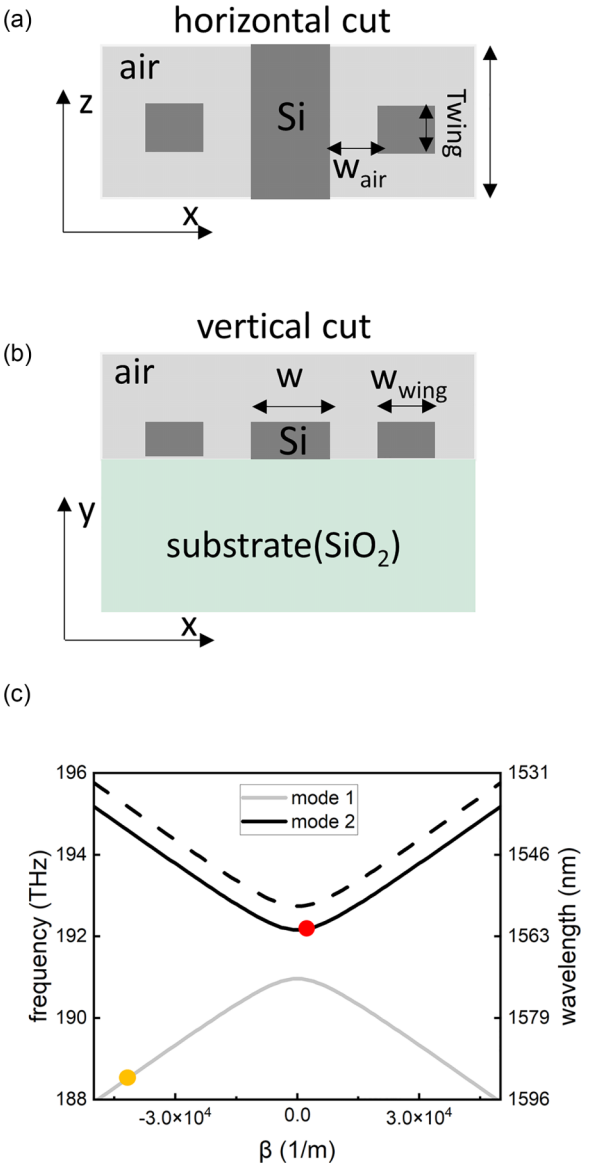

FIG. 2. Schematic of the 1 mm-long silicon waveguide with a periodic perturbation: (a) horizontal cut and (b) vertical cut. The silicon slab height and width are 220 and 500 nm, respectively. The height, width (W_{wing}), and thickness T_{wing} of the silicon wings are 220, 220, and 150 nm, respectively. The air gap between the silicon waveguide and the wings is $W_{air} = 40$ nm, and the lattice constant a is 330 nm. (c) Band diagram of the periodic waveguide approximated by two hyperbolas. The hyperbolic dispersion equation could be found in the later simulation section. The black and gray curves correspond to the upper and lower bands, and the dashed curve to the perturbed upper band, whereas the perturbed lower band is not shown. Orange and red circles indicate the proposed pump and signal frequencies at the input, respectively.

II. EXPERIMENT

A. Design and manufacture of silicon Bragg waveguide

To demonstrate the optical push broom effect on a chip, a silicon Bragg waveguide with periodic wings is designed. A schematic of the waveguide design is shown in Figs. 2(a) and 2(b). The three-dimensional (3D) schematic of the designed

periodic unit of the waveguide can be found in Appendix B1. Figure 2(c) presents the band diagram of the waveguide approximated by a hyperbolic curve, which will be introduced in later numerical simulations. A qualitative comparison between the applied hyperbolic approximation and calculated dispersion by the CST Studio Suite can be found in Appendix B3. Solid black and gray lines represent the upper and lower branches of the dispersion relation, respectively, while the dashed black line represents the shifted band due to the presence of the refractive index front. The slow light signal should be positioned at the band edge, and the fast pump at the straight branch of the dispersion relation. Technically, if we had positioned both the pump pulse and the signal wave on the upper branch of the dispersion relation, it would have been challenging to detect the blueshifted signal due to frequency overlap with the pump. Therefore, we positioned the pump frequency on the nondispersive part of the lower branch of the dispersion relation [orange circle in Fig. 2(c)].

The employed silicon waveguide was fabricated on a silicon-on-insulator substrate with slab height of 220 nm and a width of 500 nm. The patterns were exposed on a spin-coated AR-P 6200.13 electron-beam photoresist by using electron-beam lithography. Afterwards, it was transferred into the silicon slab by using an inductively coupled plasma dry etching. The residual photoresist was removed by the oxygen plasma etching and a microresist remover 1165. A scanning electron microscopy (SEM) image of the fabricated waveguide is shown in Fig. 3(a).

Light is coupled into and out of the Bragg grating using two grating couplers in combination with a single-mode fiber. Each grating coupler measures 20 μm in length and 12 μm in width and features a 400 μm adiabatic taper, gradually transitioning to a 500-nm-wide waveguide [44]. The structure of the grating is composed of air hole rows embedded in silicon. This coupler exhibits a 3 dB bandwidth of 30 nm, with an optimized peak coupling wavelength at 1570 nm and a minimum coupling loss of approximately 7 dB per coupler. Further details on the waveguide design, its 3D schematic, and the fabrication process can be found in Appendix B1. The measured linear transmission (including coupling losses) and the group index of the TE-mode for the 1-mm-long silicon Bragg waveguide are presented in Figs. 3(b) and 3(c). The overall shape of the transmission curve outside of the band-gap region is due to the transmission characteristics of the grating coupler. The spikes in the transmission curve are caused by the Fabry–Pérot oscillation at the input and output of the periodic waveguide. For group index measurements, the delay of a weak pulse with about 0.4 nm bandwidth is measured by an optical sampling oscilloscope (The measured temporal profiles are shown in Appendix B2). This measurement disregards the Fabry–Pérot oscillations and tracks only the first transmitted pulse. As can be seen, the group index increases as the wavelength approaches the band edge.

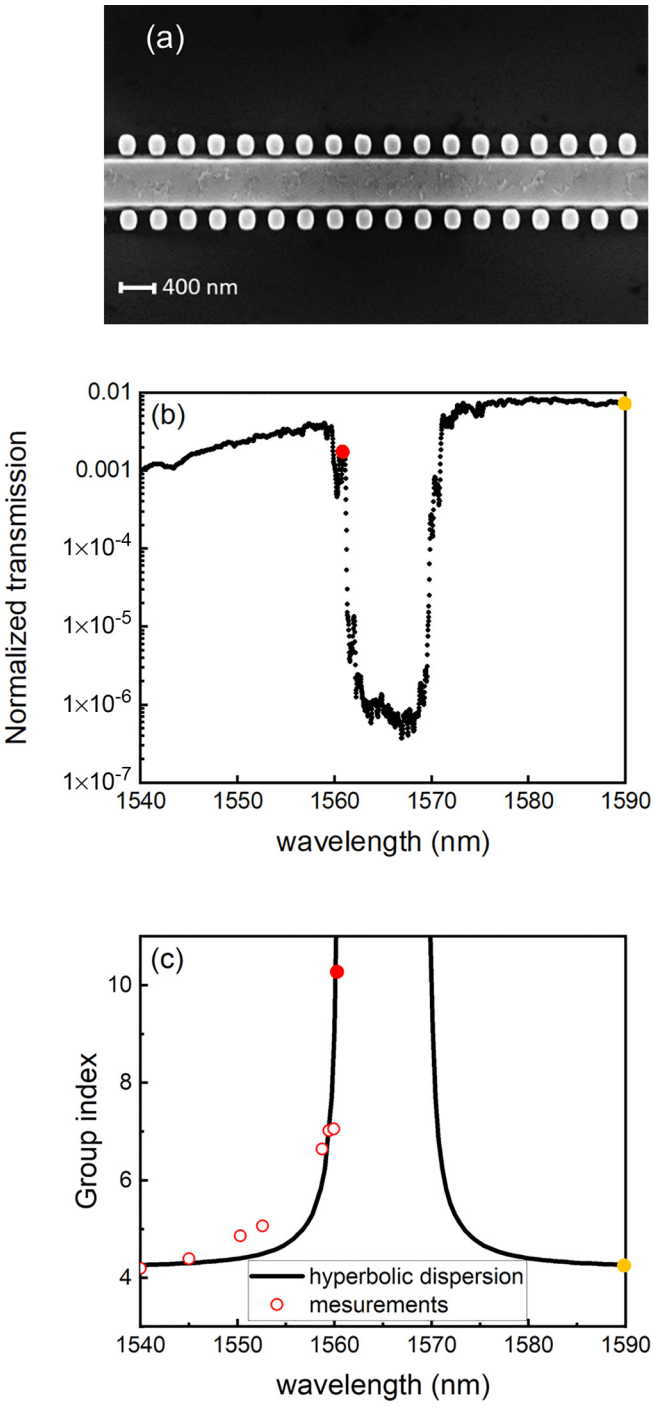

FIG. 3. Characteristics of the fabricated silicon Bragg waveguide. (a) SEM of the waveguide. Structure on the waveguide surface might come from the residual photoresist. It has a weak effect on transmission due to the small amplitude of the TE-mode fields at the upper interface of the waveguide. (b) Normalized transmission on a log scale. (c) Group index evaluated from pulse delay measurements (dots) and the hyperbolic dispersion curve approximation (black curve). Particularly, solid red and orange dots indicate the wavelengths chosen for experiments of the initial signal (1561 nm) and pump (1590 nm) wavelengths, respectively.

B. Pump and probe measurements

An optical push broom is experimentally demonstrated in the above chip with pump-probe measurements. A mode-locked fiber laser (Menlo system) with a 100 MHz repetition rate delivers pulses of approximately 100 fs duration with a wide spectrum ranging from 1500 to 1610 nm. The output is split between two grating filters with adjustable bandwidth and center frequency, followed by an erbium-doped fiber

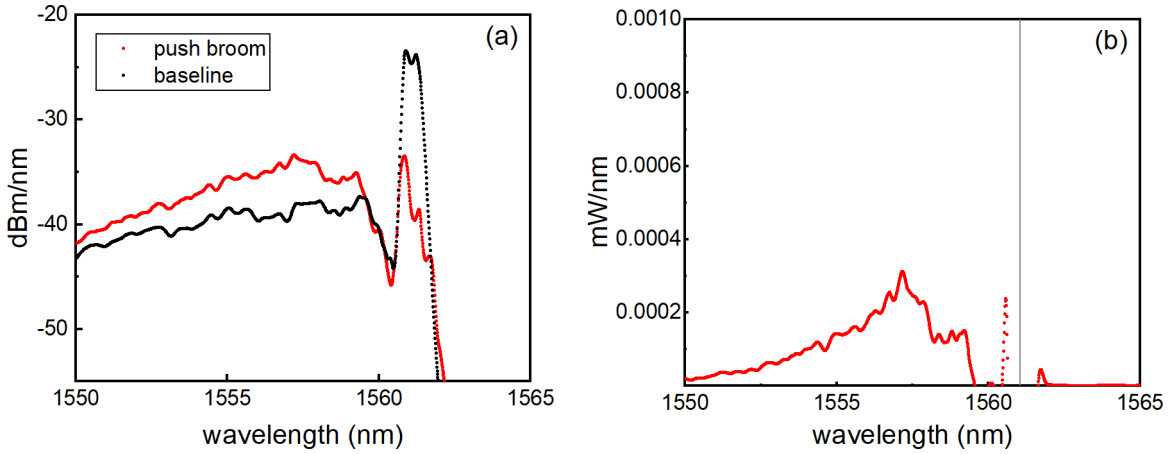

FIG. 4. (a) Unaltered output signal at 1561 nm (black curve) while pumping at 1590 nm and applying a large optical delay such that the pump pulse does not catch up with the signal. Optical push broom takes place when shifting the pump pulse close behind the signal pulse at the waveguide input, and allowing the pump to approach and collect the signal inside the waveguide (red curve). (b) To remove the ASE noise, the spectra in panel (a) were converted to a linear scale, and then the baseline spectrum was subtracted from the pushbroomed signal spectrum. The vertical straight line denotes the original signal.

amplifier. The signal pulse centered at 1561 nm with a duration of 10 ps and average power of 5 mW and the pump pulse centered at 1590 with 2 ps duration and 100 mW average power are launched into the waveguide successively, with a delay controlled by a line delay stage (General Photonics, MDL002). At these wavelengths, the group indices expected from the hyperbolic dispersion [as shown in Fig. 3(c)] are 10.3 for signal and 4.2 for pump, respectively. The pulse duration control is achieved by tuning the filter bandwidth and is checked by an autocorrelator (APE, pulseCheck 150). A 0 ps delay is manually set when the maximal frequency shift of the signal peak position is observed. It should be mentioned that this zero definition does not mean that the signal and pump pulses enter the Bragg waveguide at the same time. The output light is collected and analyzed by an optical spectrum analyzer (Ando, AQ6317). The switch on-off of the optical push broom effect is achieved by delaying the pump pulse with respect to the signal pulse, instead of turning on-off the pump pulse. In this way, the possible heat-induced perturbation of refractive index by pump illumination stays constant and could be ignored. Also, as we consider frequency shifts as a function of time delay, the pump pulse interaction with any cw signal, such as amplified spontaneous emission noise, can be excluded as a reason for the observed new frequencies. More detailed information about the experimental setup can be found in Appendix A.

We have to mention also that self-phase-modulation causes a temporally varying instantaneous frequency of the pump. This way, an initial nonchirped pump pulse acquires a frequency chirp. Still, this frequency chirp does not significantly change the pulse envelope, thus, also the free carrier front shape, as the pump is propagating at the frequency with negligible dispersion.

III. RESULTS AND DISCUSSION

A. Frequency shift and spectral broadening

Figure 4 shows the signal spectra with the maximum frequency shift, which is obtained when the delay between signal and pump is vanishing, thus the signal travels inside the front for the maximum time and propagation distance. The black curve in Fig. 4(a) represents the original spectrum serving as the baseline, which is obtained by applying a large delay to the pump pulse, such that the pump can never catch up with the signal inside the silicon Bragg grating. Conversely, the red curve illustrates the spectrum's alteration attributable to the push broom effect, achieved by reducing the delay to an optimal value and setting it to 0 ps. Notably, the original signal's disappearance at 1561 nm is coupled with a frequency shift toward a lower wavelength and a broadening of the pulse spectrum. To mitigate the amplified spontaneous emission (ASE) noise emanating from both the pump and signal light, the data represented by the two curves in Fig. 4(a) were transformed into a linear scale, subsequently subtracted, and the results are presented in Fig. 4(b). This figure intuitively demonstrates the spectral shifting and broadening of the converted pulses within the 1550–1560 nm range. Furthermore, a minimal residual presence around 1561 nm suggests that nearly all signal energy has interacted with the front. One should note that a weak pump is insufficient to induce a band diagram shift required for trapping. Once the pump power exceeds the threshold, further increase of the pump power produces a refractive index front with a larger slope, leading to a larger frequency shift. In this report, we applied the maximum pump power available in our setup to achieve maximum trapping.

Furthermore, the dependency of the optical push broom effect on the delay between signal and front is explored by adjusting the timing of the pump pulse, as depicted in Fig. 5(a). A 0 ps delay, defined as the point at which the maximum push broom effect occurs, causes the longest joint travel time and distance of signal and pump, thus yielding the most pronounced frequency shift and spectral broadening. With increasing delay, the pump light enters the waveguide later, intersecting with the signal light only after the elapsed delay time. This results in a diminished duration for the two pulses to travel together, progressively weakening the frequency shift by the push broom effect, which is proportional

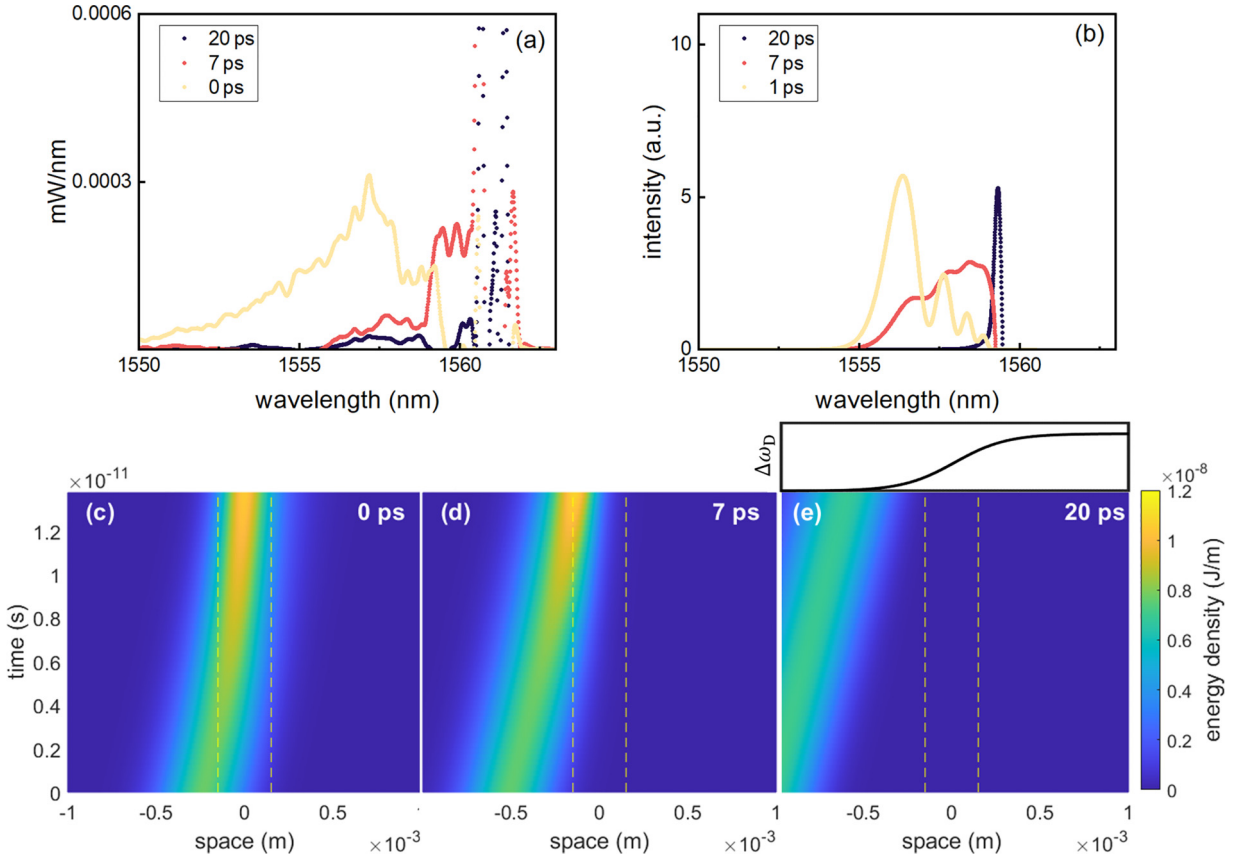

FIG. 5. (a) Signal wavelength distribution for different time delays between pump and signal from experiments and (b) the corresponding split-step Fourier method calculations prepared as a subtraction of the converted and original signal. The delay of 0, 7, 20 ps represent a full conversion, partial conversion, and nearly zero conversion, respectively. The oscillations in panel (b) for the delay of 0 ps originates from the signal light being partially located inside the front already at the input of the waveguide. The corresponding signal pulse evolution for three delays is shown in panels (c)–(e). The color represents the linear energy density. The reference frame of the front is used, where the straight dashed line indicates the front width. In particular, the black curve at the top of panel (e) schematically shows the dispersion shift $\Delta\omega_D$ as a function of position around the front.

to the time spent inside the slope of the refractive index perturbation [9]. The reduction in the frequency shift can also be explained by the Fourier transform induced by the optical push broom [12]. Three distinct delays—0, 7, and 20 ps—were chosen for analysis and are presented in Fig. 4(a). These curves correspond to the signal pulse being fully converted, partially converted, and experiencing an almost negligible interaction, respectively. The dashed straight line represents the wavelength of the input pulse. An increase in delay leads to a reduction in frequency shift, in alignment with theoretical predictions. Another indication of the partial conversion is observed in the residual power at the input wavelength, consisting of unconverted original signal components. This is more clearly illustrated by series measurements at different delays in Appendix D. The residual signal pulse at the original wavelength is shorter than the original pulse and thus results in a slight broadening of the original signal spectrum, which is observed as sharp peaks around the initial frequency in Fig. 4(b).

In the case of optimal delay, the spectral broadening of the converted signal indicates the compression in the time domain. However, a direct measurement of the compressed pulse was not possible due to its low power, which is mixed with a strong pump pulse. An estimation of this compression will be given in the next section, together with numerical simulations.

B. Numerical simulations

To better interpret the experimental results, the numerical simulations for the pulse have been introduced and shown together with the experiment in Figs. 5(b)–5(e) for comparison. The interactions between the signal light and the moving index front were modeled using a slowly varying envelope approximation as follows [45–47]:

$$\frac{\partial A(t,z')}{\partial t} = (v_f - v_{g0})\frac{\partial A}{\partial z'} + \sum_{n=2}^{N} i^{(n-1)}\frac{\omega_n}{n!}\frac{\partial^n A}{\partial z'^n} + i\Delta\omega_D(z')A. \tag{1}$$

Here, $A(t,z')$, v_f, and v_{g0} represent the signal envelope function, group velocity of the front, and group velocity of the signal at wave number $\beta = 0$, respectively, where β is defined with respect to the reference wave number. In our case, we chose the reference wave number at the band gap of the Bragg grating and thus $v_{g0} = 0$. The coefficients $\omega_n = \partial^n\omega/\partial\beta^n$ are the dispersion coefficients coming

from the Taylor series expansion of the dispersion function $\omega(\beta)$ at $\beta = 0$, and $\Delta\omega_D(z')$ is the local shift of the dispersion relation due to the refractive index perturbation. The spatial coordinate $z' = z - v_f t$ represents the position in the frame of the stationary front and $A(t, z')$ represents the temporal evolution of the signal envelope in space with respect to the front. The spectral distribution of the signal can be obtained by the spatial Fourier transform of the envelope and conversion from spatial frequency into temporal frequency [12].

This differential equation is solved numerically by the split-step Fourier method (SSFM) [48]. It allows us to consider any given dispersion without Taylor expansion. We approximate the dispersion of the Bragg grating by the hyperbolic function $\omega(\beta) = \omega_{PBG} + \Delta\omega_{PBG}(1 + [\beta^2/\Delta\beta_{PBG}^2])^{1/2}$, where ω_{PBG} and represent the central frequency of the band gap, $\Delta\omega_{PBG}$ is half of the band gap, and $\Delta\beta_{PBG} = \Delta\omega_{PBG}/v_{g\infty}$ is the parameter chosen to define the group velocity of light away from the band gap as $v_{g\infty}$, where the hyperbolic function is converging to a straight line. For our waveguides, the group velocity away from the band gap is approximately $v_{g\infty} = c/4.2$. The effect of this dispersion is calculated in reciprocal space as the phase accumulates with time according to $\omega(\beta)$. The viability of the approximation by the hyperbolic dispersion curve is also confirmed by a numerical simulation of the band diagram in CST Studio Suite (details shown in Appendix B3). The index front and the corresponding shift of the dispersion relation $\Delta\omega_D$ are described by a hyperbolic tangent function centered at $z' = 0$: $\Delta\omega_D = \Delta\omega_{max}[1 + \tanh(z'/\Delta z_f)]$, where $\Delta\omega_{max}$ and Δz_f represent the pump-induced maximum band diagram shift and front half-width, receptively [49]. As evaluated in previous reports [36,50], free carriers and the Kerr effect in silicon result in a negative and positive index change, respectively. In our case, the free carrier contribution dominates the effect and also defines the shift of the dispersion relation after the front, as the Kerr effect is instantaneous and vanishes with the pump, whereas the induced free carriers have a lifetime much longer than the pulse duration. Here, a simple hyperbolic tangent function was applied to simulate the overall effect decided by the end state. It should also be mentioned that the pump pulse decays with propagation in the waveguide due to two-photon and free carrier absorption, leading to the subsequent attenuation of the index front. Also, a 60% additional loss for the signal pulse due to these absorptions was observed, as shown in Appendix E. Here, a constant-index front was simulated for simplification. The minor difference due to front decay is also simulated and shown in Appendix E.

The three most important parameters for SSFM calculations are the maximal frequency shift of the dispersion relation due to excited free carriers (0.4 THz) and the group velocity of the pump ($c/4.2$) and signal ($c/10.3$). A detailed explanation for the parameters and related measurements is given in Appendix E. The signal pulse has initially a Gaussian profile in the time domain $B(t, z_0)$ at the position $z_0 = 0$ and is converted into the spatial distribution $A(t_0, z)$ at time $t_0 = 0$ for later SSFM calculations with temporal evolution of spatial profiles. After propagating the time required to reach the output, the spatial profile is converted back to the time domain for compression estimation. The conversion between temporal frequency distribution at position z, $B(\omega, z)$, and spatial frequency distribution at time t, $A(t, \beta)$, was achieved by considering the connection between spectral linear energy density and spectral power density: $|B(\omega)|^2 = |A(\beta(\omega))|^2/v_g(\omega)$ [12]. Additionally, a phase shift $e^{i[\omega t + \beta(\omega)z]}$ is implemented to correct the phase to any chosen position z for the given spatial envelope at time t. Besides, we correct the input and output spectral power density by the reflection coefficient at the input and output sections of the Bragg waveguide, approximated by the group-velocity mismatch $v_g(\omega)/v_{g\infty}$.

Building on the aforementioned analysis, the spectra at various delays have been computed and are presented in Fig. 4(b). Notably, the oscillations—which are most pronounced at a 0 ps delay—stem from the interference caused by portions of the signal light initially positioned within the front at the waveguide entry. Similar to the experiment, 0 ps is defined as the delay at which the strongest frequency shift is observed. The observed slight shift in the signal wavelength, compared with experimental results, can be attributed to discrepancies between the estimated parameters and actual conditions. Despite these discrepancies, the calculations successfully replicate the experimental observations regarding frequency shift and spectral broadening. Furthermore, pulse profile evaluations are depicted in Figs. 4(c) to 4(e), offering an intuitive view of the push broom effect under different delay conditions. Here, the pulse is injected with 0, 7, and 20 ps delays, and the dashed lines mark the front width. It becomes evident that an increase in delay leads to the signal light encountering the front later, resulting in diminished frequency shift and compression.

SSFM calculations provide a basis for estimating pulse compression attributable to the push broom effect. The compression factor is determined by the ratio of the pulse full width at half maximum (FWHM) at the input to that at the output ($\tau_{input}/\tau_{output}$). In this simulation, the maximum compression factor achieved is 2.5. This temporal compression might not be obvious from Fig. 4, as the signal should be first converted into the laboratory frame. Even if the signal pulse is not compressed in space, it is compressed in time as it is accelerated by the front.

Moreover, the maximal compression achievable in this waveguide can be estimated. The compression factor is inversely proportional to the square of the initial signal duration [12]. The 10 ps experimental duration represents a balanced choice. While a longer duration would result in a stronger signal compression, it could obscure the delay dependence as a large portion of the signal will already be inside the front at the input of the Bragg waveguide. Our choice of 10 ps duration allows for a clear observation of the delay-dependent dynamics while still achieving adequate compression. The maximal possible duration for the signal that can be collected by the front is

$$\tau_{max} = L\left(\frac{|n_g^s - n_g^f|}{c}\right), \tag{2}$$

where L is the length of the waveguide, and n_g^s and n_g^f represents the group index of the signal and front wavelengths. From this equation, a 20 ps signal pulse can be fully collected and compressed in a 1 mm waveguide if the front does not decay with propagation. Consequently, the maximal compression factor under the inverse square law could be estimated to be 10 [12]. The pulse compression is also connected to spectral broadening. Experimental data indicate a more significant broadening than predicted by SSFM calculations [see Fig. 4(a) and 4(b), implying that the experimental front might be stronger, as assumed in the SSFM. Notably, as addressed theoretically [12], in the case that one ideally applies an infinite waveguide with a nondecaying front, the signal pulse would still be finitely compressed but continuously varying in frequency.

IV. CONCLUSION

In conclusion, we have successfully demonstrated the trapping and manipulation of a signal pulse within a moving index front inside a 1-mm-long silicon Bragg waveguide. The slow signal pulse is approached by the fast front, accelerated, and collected in the front region. The effect is demonstrated experimentally by the disappearance of the signal at the original frequency and appearance of a wide shifted spectrum. Additionally, the evolution of the pulse was modeled using the slowly varying envelope approximation and numerically resolved through the split-step Fourier method. The direct measurement of the pulse durations after the push broom setup was not possible due to the weak intensity of the transmitted signal pulse and mixing with the pump pulse. In simulations, we could well reproduce the experimentally observed frequency shifts and thus could estimate a compression of approximately 2.5 times. The potential for achieving even higher compression factors exists and can be readily explored by employing a sharper moving front, extending the waveguide length, and switching from the lossy free carrier effect to the Kerr nonlinearity. This research paves the way for advanced manipulation of light pulse temporal profiles, offering an efficient pathway to one-step pulse compression.

ACKNOWLEDGMENTS

We would like to acknowledge the sponsorship from Dassault Systems with their CST Studio Suite software. B.Z., M.A.G., M.E., and A.Y.P. would like to acknowledge the German Research Foundation (DFG) (Projects No. 392102174 and No. 493328928) for its financial support. H.L., X.C., and J.L. acknowledge the support from National Natural Science Foundation of China (NSFC) (Project No. 11761131001).

The authors declare no conflicts of interest.

DATA AVAILABILITY

The data that support the findings of this article are not publicly available. The data are available from the authors upon reasonable request.

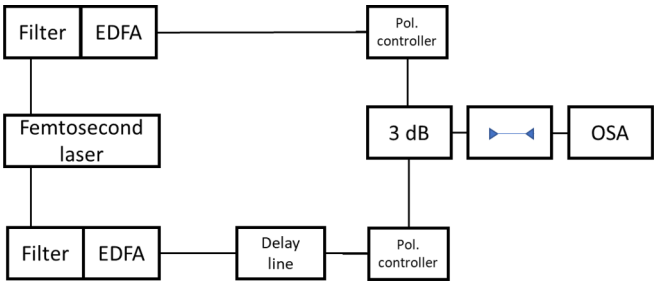

FIG. 6. Schematic of the experimental setup. EDFA, erbium-doped fiber amplifier; Pol. controller, polarization controller and 3 dB, 50:50 beam combiner; OSA, optical spectrum analyzer. All solid lines represent fiber coupling.

APPENDIX A: EXPERIMENTAL SETUP

The experiment is arranged as displayed in Fig. 6. A mode-locked fiber laser (Menlo system) with a 100 MHz repetition rate delivers pulses of approximately 100 fs duration. The output is divided into pump and signal branches with adjustable bandwidth and center frequency (by filter, Santec, OTF-350), followed by an erbium-doped fiber amplifier (EDFA). A 2-ps optical pump centered at 1590 nm has an average power of around 100 mW, and the polarization is controlled by a polarization controller (Thorlabs, FPC561) for an optimized coupling into the subsequent waveguide grating. The signal light is tunable from 1500 to 1590 nm with a duration ranging from 2 to 30 ps. Pulse duration is measured by an autocorrelator (APE, pulseCheck 150). The average power of the signal light after the EDFA is around 10 mW. Additionally, a delay line (GeneralPhotonics, MDL-002) is added after the EDFA to adjust the time delay of the signal pulse, which allows us to control the delay within 550 ps. Subsequently, two pulses (pump and signal) are combined through a 50:50 (3 dB) beam combiner, which is then fiber-coupled to the grating coupler. The optical spectra are measured by the optical spectrum analyzer (Ando AQ6317). An SEM of the grating coupler is shown in Fig. 7.

APPENDIX B: WAVEGUIDE DESIGN AND CHARACTERIZATION

1. Details of the waveguide and its coupler

The silicon Bragg waveguide and its coupler were fabricated on a Silicon-on-Insulator (SOI) substrate, featuring a 220-nm-thick silicon layer. The patterning process began with the application of AR-P 6200.13 electron-beam photoresist, spin-coated onto the substrate. Subsequent patterning employed electron-beam lithography (EBL) to precisely define the waveguide structures. These patterns were then etched into the silicon layer using inductively coupled plasma (ICP) dry etching, ensuring accurate transfer of the intricate designs. Following this, residual photoresist was eliminated via oxygen plasma etching and a micro resist remover, preparing the surface for the final fabrication steps. The resulting grating couplers, designed for optimal efficiency in coupling between single-mode fibers and the silicon chip, feature a 20 μm length and 12 μm width. These couplers incorporate apodized photonic crystal columns to facilitate precise control over the

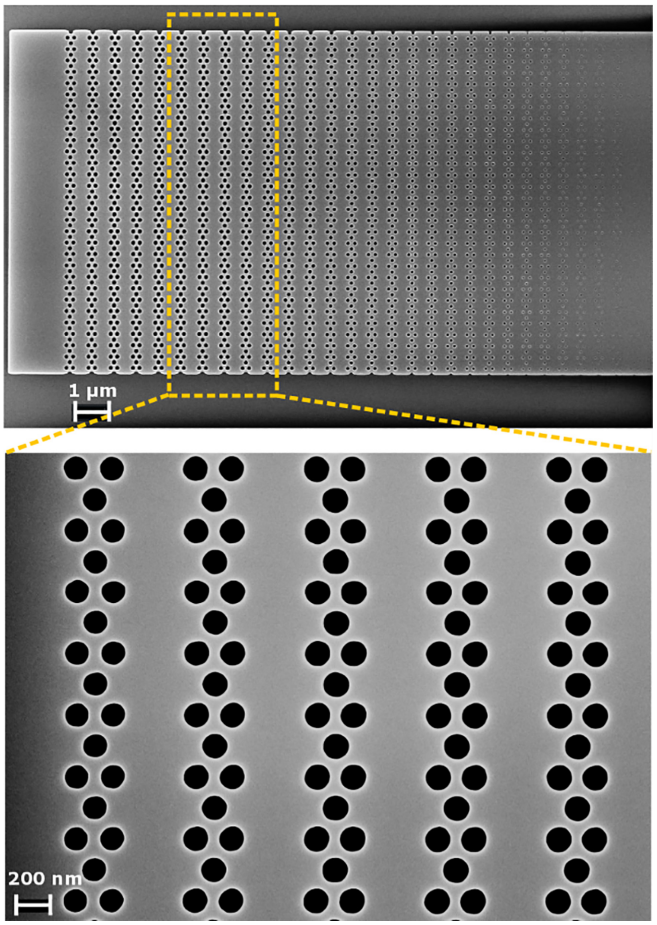

FIG. 7. SEM image of the grating coupler.

coupling process [44,51]. Notably, the coupler achieves a 3 dB bandwidth of 30 nm, centered at a peak wavelength of 1570 nm, while maintaining a minimal coupling loss of 7 dB per coupler.

Moreover, a 3D schematic of the Bragg waveguide is shown in Fig. 8, which shows the structural parameters of the waveguide.

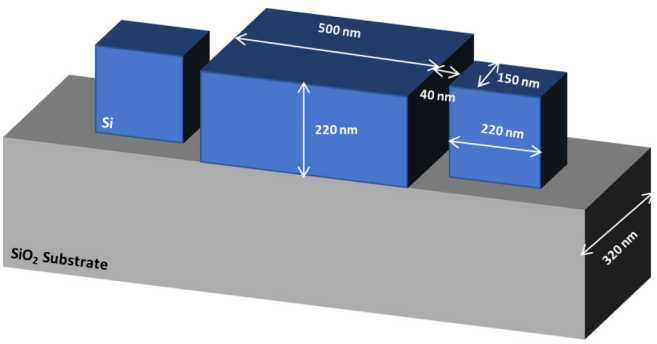

FIG. 8. 3D schematic of the designed periodic unit of the waveguide.

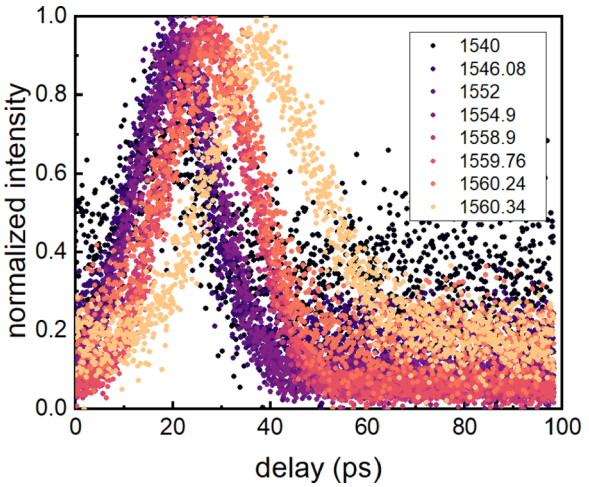

FIG. 9. Normalized intensity of the temporal profile of signal pulse at different wavelengths. As the wavelength increases, the relative delay increases, which shows the decreasing group velocity when approaching the band gap.

2. Group index measurement on the waveguide

The group index shown in Fig. 3(c) was evaluated from the relative delay measurements by oscilloscope (Agilent 86100D sampling oscilloscope and the optical module 86116C with optical bandwidth 65GHz, time interval accuracy 1 ps and time interval resolution 62.5 fs), of which the temporal profiles at different wavelengths are shown in Fig. 9. The relative delay of each signal pulse to pump pulse was decided by a Gaussian fit of the corresponding temporal profile. Afterward, the delay was converted into group index by assuming the group index far from the band gap equals 4.2, which is confirmed by a CST simulation on a blank Si waveguide. As shown in Fig. 9, the delay of the signal pulse increases while approaching the band gap.

3. Dispersion relation from CST simulation and hyperbolic approximation

In this paper, we use a hyperbolic approximation of the dispersion function of the Bragg grating: $\omega(\beta) = \omega_{\mathrm{PBG}} + \Delta\omega_{\mathrm{PBG}}(1 + [\beta^2/\Delta\beta^2_{\mathrm{PBG}}])^{1/2}$, where ω_{PBG} represents the central frequency of the band gap, $\Delta\omega_{\mathrm{PBG}}$ is the half of the band gap width, and $\Delta\beta_{\mathrm{PBG}} = \Delta\omega_{\mathrm{PBG}}/v_{g\infty}$ is the parameter chosen to define the group velocity of light with a frequency away from the band gap as $v_{g\infty}$. These parameters are extracted from measurements on the waveguide.

At the same time, we can calculate the dispersion relation of the Bragg waveguide using geometrical parameters defined in the caption of Fig. 2 (using CST Studio eigenmode solver with periodic boundary conditions). However, the calculated band-gap width and band-gap position deviate strongly from the measured values. Thus, we expect that manufactured samples have dimensions that deviate from the design parameters.

Still, the hyperbolic function is a very good approximation of the band diagram of the Bragg waveguides. To clarify and examine the qualitative difference between calculated dispersion and hyperbolic dispersion, we inserted the band-gap parameters (ω_{PBG}, $\Delta\omega_{\mathrm{PBG}}$, and $\Delta\beta_{\mathrm{PBG}}$) from simulated

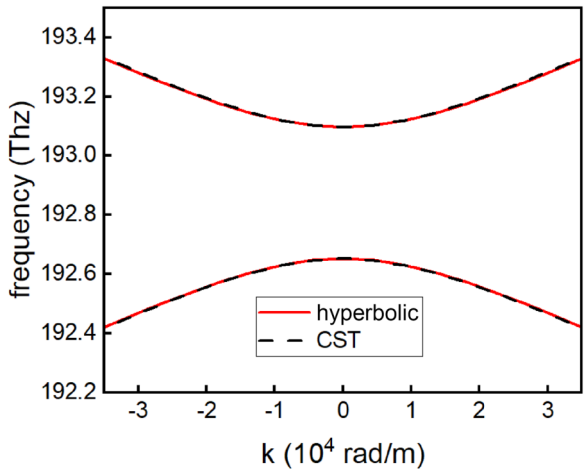

FIG. 10. The diagram comparison between a hyperbolic approximation (solid line) and the CST calculation (dashed line).

dispersion into the hyperbolic function. As shown in Fig. 10, the modified hyperbolic approximation well reproduced the dispersion function calculated with CST Studio. This is also expected for Bragg gratings where forward and backward waves are coupled by a weak periodic perturbation.

APPENDIX C: ENERGY ACCUMULATION IN THE OPTICAL PUSH BROOM EFFECT

To illustrate the energy accumulation characteristic of the optical push broom effect, we also analyzed the spectrum resulting from cross-phase modulation (XPM) but without the group index mismatch (GVM) (trapping case), depicted in Fig. 11. The signal is shifted to 1547 nm, aligning the velocity of the signal pulse with that of the pump light. Consequently, the signal pulse "surfs" on the index front rather than being collected and compressed. Figure 11 reveals that XPM

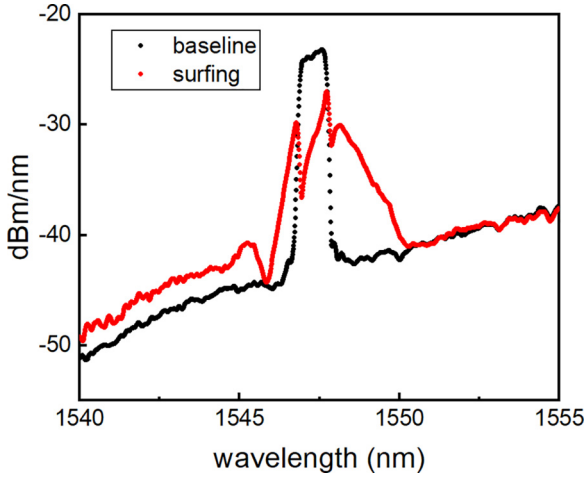

FIG. 11. Signal spectra for the case when signal group velocity is matched to pump group velocity. The black line (baseline) is measured with a large delay between signal and pump so that they do not interact. The red line (surfing) represents the case when pump and signal copropagate in the waveguide, and the signal experiences XPM without GVM.

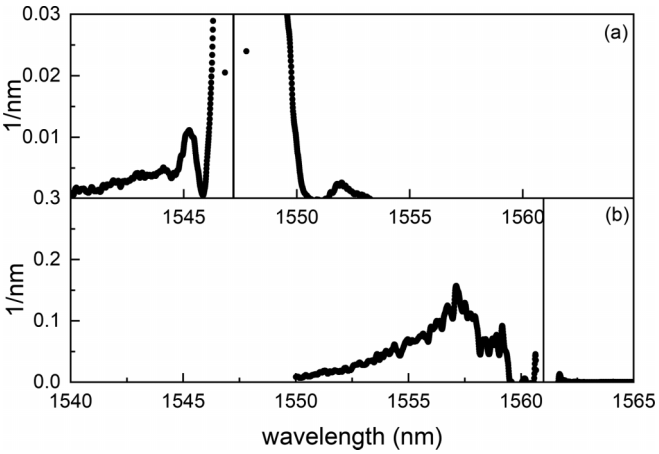

FIG. 12. Comparison of the conversion efficiency between the (a) no GVM and (b) with GVM (trapping case). Note the intensity scale for the trapping case (b) is expanded tenfold to accommodate its significantly higher intensity. The straight vertical line indicates the input signal wavelength.

without GVM induces frequency shifts to higher and lower frequencies, stemming from the signal pulse interacting with both the positive and negative slopes of the refractive index perturbation induced by the pump pulse.

To elucidate the spectral changes more clearly, the spectra in Fig. 11 were converted to a linear scale and subtracted, with the results presented in Fig. 12(a). For comparative analysis, the push broom effect, discussed in the main text, is also graphically represented alongside in Fig. 12(b). The spectral efficiency on the y axis—defined as the power per wavelength unit normalized to the transmitted power of the signal pulse at the output (1/nm)—facilitates a direct comparison between the conversion efficiencies of surfing and the push broom effect. Notably, the intensity scale for the push broom effect is expanded tenfold to accommodate its significantly higher intensity. The vertical line marking the input signal wavelength indicates that, in Fig. 12(a), XPM without GVM generates a modest peak at 1546 nm. Conversely, the push broom effect produces a substantially broader peak with an intensity roughly 15 times greater, as shown in Fig. 12(b). This marked increase in conversion efficiency underscores the ability of the push broom effect to accumulate energy, whereby the front traps and accelerates the signal pulse. Additionally, the residual signal at the input wavelength in the case of XPM without GVM, compared with the near-total conversion of the input signal to a new frequency under the push broom effect, further highlights the latter's efficiency.

APPENDIX D: OPTICAL PUSH BROOM SPECTRA VS DELAY

In the main text, for the sake of simplicity, we presented three representative spectra corresponding to delays of 0, 7, and 20 ps. These were chosen to exemplify the signal pulse undergoing almost complete conversion, partial conversion, and negligible conversion. Additional spectra have been compiled and are displayed in Fig. 13. Consistent with the presentation style of the main text, Fig. 13(a) showcases the original spectra, while Fig. 13(b) presents the results of linear

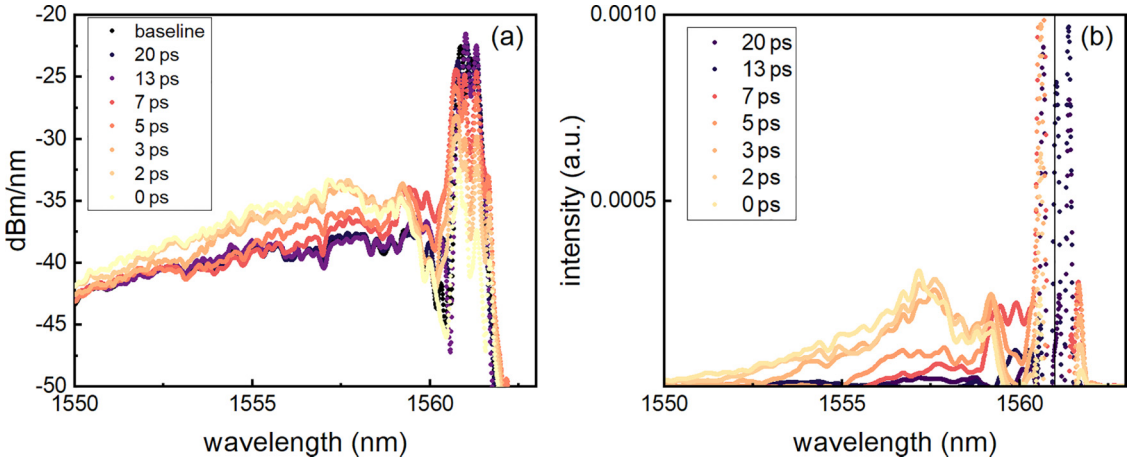

FIG. 13. (a) Signal spectra after interaction with the front at different time delays and (b) difference between the signal spectra and the baseline in linear scale.

subtraction. One can clearly see that the frequency shift by the push broom effect becomes weaker when increasing the delay between pump and signal pulses. Besides, the residual energy at the original signal wavelength is also increasing with growing delay.

APPENDIX E: PARAMETERS FOR NUMERICAL SIMULATIONS BY SSFM

The propagation of pulses along the waveguide is modeled by Eq. (1) and solved numerically by the split-step Fourier method:

$$\frac{\partial A(t,z')}{\partial t} = (v_f - v_{g0})\frac{\partial A}{\partial z'} + \sum_{n=2}^{N} i^{(n-1)}\frac{\omega_n}{n!}\frac{\partial^n A}{\partial z'^n} + i\Delta\omega_D(z')A. \tag{E1}$$

Here, $A(t,z)$, v_f, and v_{g0} represent the signal envelope function, group velocity of the front, and the group velocity of the signal at $\beta = 0$, respectively. In simulation, the signal is launched with a shifted β value, by fitting the experimentally measured group velocity to the point on the estimated hyperbolic dispersion relation. The signal group velocity is obtained as a difference in the speed of the pump and signal light measured indirectly by an optical oscilloscope. The front speed v_f is obtained as a group velocity away from the band gap simulated by the eigenmode solver of CST Studio Suite. The simulation gives the group index n_f far from the band gap as 4.2. The simulation time (the time for the pump light to pass the waveguide) is determined by the pump speed and the waveguide length.

Another critical parameter in our study is the frequency shift of the dispersion relation due to free carrier generation. This parameter essentially determines the extent of the frequency shift observed. While direct measurement poses challenges, we can approximate its magnitude by assessing the free carrier absorption effects. To this end, we analyzed the transmitted power of the signal pulse at the output of the waveguide across various delays [50], as depicted in Fig. 14. Unlike the push broom effect, the signal light was set at 1546 nm where signal propagates with the same group velocity as pump and frequency changes are caused by cross phase modulation (XPM). The signal pulse duration was 10 ps. It is important to note that the power contributions from the pump light have already been subtracted from these measurements. The strong drop of output power close to 0 delay corresponds to the cross two-photon absorption (one photon from signal and one from pump) plus free carrier absorption, whereas the loss at larger negative delays indicates solely free carrier absorption. Based on the observed reduction in output power—approximately 25% in our experimental setup—we can infer the degree of free carrier absorption.

Assuming the waveguide mode is concentrated in silicon, we can equalize the waveguide absorption coefficient to the material absorption coefficient. The obtained absorption coefficient α can then be used to estimate the generated free carrier

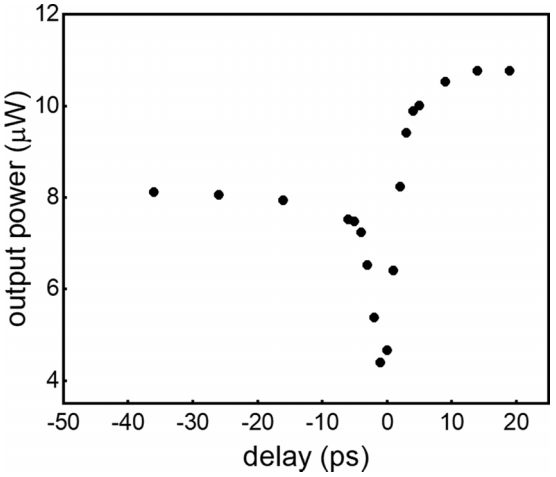

FIG. 14. Transmitted signal power vs optical delay for signal at 1546 nm. A delay of 0 ps is set when the maximal frequency shift by XPM is observed. Positive delay times represent the signal pulses that are running ahead of the pump, in which the drop at 0 ps delay corresponds to two-photon absorption plus free carrier absorption. The transmission loss for negative delays compared with positive delays is solely caused by free carrier absorption, where the pump is running ahead of the signal.

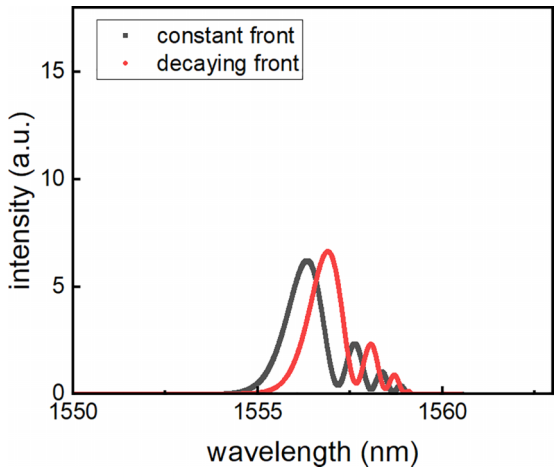

FIG. 15. SSFM simulations using a constant front (black) and a decaying front (red). A decaying front results in a weaker frequency shift but keeps the same spectral features.

concentration ΔN:

$$\Delta\alpha = \sigma \Delta N, \tag{E2}$$

where $\sigma = 1.45 \times 10^{-17}(\lambda/1.55)\ \mathrm{cm}^2$, λ is the wavelength, ΔN represents the free carrier absorption cross-section, wavelength and free carrier concentration, respectively [50]. Afterward, the change on refractive index could be expressed as [52]:

$$\Delta n = -(e^2\lambda^2/8\pi^2c^2\varepsilon_0 n)[\Delta N_e/m^*_{ce} + \Delta N_h/m^*_{ch}]. \tag{E3}$$

where e, ε_0, n is the electron charge, permittivity of free space and refractive index of Si, respectively. ΔN_e and m^*_{ce} represent the change of electron concentration and the effective mass of electrons, while ΔN_h and m^*_{ch} correspond to the change of hole concentration and the effective mass of holes. ΔN_e and ΔN_h can be estimated from ΔN by $\Delta N_e = \Delta N^x$ and $\Delta N_h = \Delta N^y$. The coefficients x and y are experimentally fitted to be 1.04 and 0.818, respectively, at 1550 nm in silicon by Soref *et al.* [52]. They have also reported that at 1300 nm, $\Delta N_e = \Delta N^{1.05}$ and $\Delta N_h = \Delta N^{0.804}$. And in Dekker's calculation [50], $\Delta N_e = \Delta N^1$ and $\Delta N_h = \Delta N^{0.8}$ are applied at 1554 nm. It is important to emphasize that the specific values chosen here do not alter the relative dependence of the push broom spectra on delay; they only make the frequency shift stronger or weaker. This flexibility allows for the adjustment of the shifted peak's position or even for fitting simulation results to match experimental observations closely. After all, the maximal band diagram shift $\Delta\omega_{\max}$ is estimated by

$$\Delta\omega_{\max}/\omega = \Delta n/n, \tag{E4}$$

where $\Delta\omega_{\max}$ stands for the frequency shifted by pump excitation. By adapting different electron (hole) concentration coefficient x (y), $\Delta\omega_{\max}$ varies within 0.161–0.486 THz. In our SSFM calculation, $\Delta\omega_{\max} = 0.4$ THz is applied to roughly fit the spectra to experimental output.

As mentioned in the main text, the pump pulse decays with propagation in the waveguide due to two-photon and free carrier absorption, leading to the reduction of the index front. We have applied a constant front for simplification. Here, the simulations with a decaying front have been performed by assigning a decaying coefficient to the shift of the dispersion relation induced by the front:

$$\Delta\omega_{\mathrm{D}} = \Delta\omega_{\max}[1 + \tanh(z'/\Delta z_{\mathrm{f}})]e^{-\alpha_{\mathrm{p}} v_{\mathrm{f}} t}, \tag{E5}$$

where α_{p} is the pump time decay coefficient, which was calculated from the spatial decay coefficient of 3 cm^{-1} estimated from the free carrier absorption in Fig. 14, and v_{f} is the velocity of the front (c/4.2). The simulation was performed at 0 ps delay and plotted together with the nondecaying-front case in Fig. 15. Compared with the nondecaying case, the decaying front produces the same spectral features but with a smaller frequency shift due to the weaker front. Thus, in the main text, we omit minor differences resulting from the decay of the front to simplify the discussion.

[1] V. R. Almeida, C. A. Barrios, R. R. Panepucci, and M. Lipson, All-optical control of light on a silicon chip, Nature (London) **431**, 1081 (2004).

[2] E. Galiffi, R. Tirole, S. Yin, H. Li, S. Vezzoli, P. A. Huidobro, M. G. Silveirinha, R. Sapienza, A. Alù, and J. B. Pendry, Photonics of time-varying media, Adv. Photonics **4**, 014002 (2022).

[3] S. Vezzoli, V. Bruno, C. Devault, T. Roger, V. M. Shalaev, A. Boltasseva, M. Ferrera, M. Clerici, A. Dubietis, and D. Faccio, Optical time reversal from time-dependent epsilon-near-zero media, Phys. Rev. Lett. **120**, 043902 (2018).

[4] D. Vercruysse, N. V. Sapra, L. Su, and J. Vuckovic, Dispersion engineering with photonic inverse design, IEEE J. Sel. Top. Quantum Electron. **26**, 1 (2020).

[5] C. Guo and S. Fan, Generation of guided space-time wave packets using multilevel indirect photonic transitions in integrated photonics, Phys. Rev. Res. **3**, 033161 (2021).

[6] M. Castellanos Muñoz, A. Y. Petrov, L. O'Faolain, J. Li, T. F. Krauss, and M. Eich, Optically induced indirect photonic transitions in a slow light photonic crystal waveguide, Phys. Rev. Lett. **112**, 053904 (2014).

[7] K. Kondo and T. Baba, Dynamic wavelength conversion in copropagating slow-light pulses, Phys. Rev. Lett. **112**, 223904 (2014).

[8] D. M. Beggs, T. F. Krauss, L. Kuipers, and T. Kampfrath, Ultrafast tilting of the dispersion of a photonic crystal and adiabatic spectral compression of light pulses, Phys. Rev. Lett. **108**, 033902 (2012).

[9] M. A. Gaafar, T. Baba, M. Eich, and A. Y. Petrov, Front-induced transitions, Nat. Photonics **13**, 737 (2019).

[10] N. G. R. Broderick, D. Taverner, D. J. Richardson, M. Ibsen, and R. I. Laming, Optical pulse compression in fiber Bragg gratings, Phys. Rev. Lett. **79**, 4566 (1997).

[11] M. A. Foster, R. Salem, Y. Okawachi, A. C. Turner-Foster, M. Lipson, and A. L. Gaeta, Ultrafast waveform compression using a time-domain telescope, Nat. Photonics **3**, 581 (2009).

[12] M. A. Gaafar, H. Renner, M. Eich, and A. Y. Petrov, Fourier optics with linearly tapered waveguides: Light trapping and focusing, APL Photonics **6**, 66108 (2021).
[13] J. B. Pendry, Air conditioning for photons, [Invited], Opt. Mater. Express **14**, 407 (2024).
[14] Z. Yu and S. Fan, Complete optical isolation created by indirect interband photonic transitions, Nat. Photonics **3**, 91 (2009).
[15] A. W. Schiff-Kearn, L. Gingras, S. Bernier, N. Chamanara, K. Agarwal, J. M. Ménard, and D. G. Cooke, Front-induced transitions control THz waves, Commun. Phys. **4**, 162 (2021).
[16] K. Kondo and T. Baba, Slow-light-induced Doppler shift in photonic-crystal waveguides, Phys. Rev. A **93**, 011802(R) (2016).
[17] B. W. Plansinis, W. R. Donaldson, and G. P. Agrawal, What is the temporal analog of reflection and refraction of optical beams? Phys. Rev. Lett. **115**, 183901 (2015).
[18] F. Meng, M. D. Thomson, and H. G. Roskos, Relativistic Doppler frequency upconversion of terahertz pulses reflecting from a photoinduced plasma front in silicon, Phys. Rev. B **90**, 155207 (2014).
[19] M. A. Gaafar, D. Jalas, L. O'Faolain, J. Li, T. F. Krauss, A. Y. Petrov, and M. Eich, Reflection from a free carrier front via an intraband indirect photonic transition, Nat. Commun. **9**, 1447 (2018).
[20] D. M. Beggs, I. H. Rey, T. Kampfrath, N. Rotenberg, L. Kuipers, and T. F. Krauss, Ultrafast tunable optical delay line based on indirect photonic transitions, Phys. Rev. Lett. **108**, 213901 (2012).
[21] K. E. Webb, M. Erkintalo, Y. Xu, N. G. R. Broderick, J. M. Dudley, G. Genty, and S. G. Murdoch, Nonlinear optics of fibre event horizons, Nat. Commun. **5**, 4969 (2014).
[22] S. F. Wang, A. Mussot, M. Conforti, A. Bendahmane, X. L. Zeng, and A. Kudlinski, Optical event horizons from the collision of a soliton and its own dispersive wave, Phys. Rev. A **92**, 023837 (2015).
[23] C. M. de Sterke, Optical push broom, Opt. Lett. **17**, 914 (1992).
[24] M. S. Jang and H. Atwater, Plasmonic rainbow trapping structures for light localization and spectrum splitting, Phys. Rev. Lett. **107**, 207401 (2011).
[25] M. J. Steel and C. Martijn De Sterke, Schrödinger equation description for cross-phase modulation in grating structures, Phys. Rev. A **49**, 5048 (1994).
[26] M. Marko, X. Li, and J. Zheng, Soliton propagation with cross-phase modulation in silicon photonic crystal waveguides, J. Opt. Soc. Am. B **30**, 2100 (2013).
[27] Y. Zhang, C. Husko, J. Schröder, and B. J. Eggleton, Pulse evolution and phase-sensitive amplification in silicon waveguides, Opt. Lett. **39**, 5329 (2014).
[28] Y. Zhang, B. J. Eggleton, T. F. Krauss, I. H. Rey, J. Schröder, S. Lefrancois, and C. Husko, Cross-phase modulation-induced spectral broadening in silicon waveguides, Opt. Express **24**, 443 (2016).
[29] P. Colman, C. Husko, S. Combrié, I. Sagnes, C. W. Wong, and A. De Rossi, Temporal solitons and pulse compression in photonic crystal waveguides, Nat. Photonics **4**, 862 (2010).
[30] J. Xia, S. Serna, W. Zhang, L. Vivien, and É. Cassan, Hybrid silicon slotted photonic crystal waveguides: How does third order nonlinear performance scale with slow light? Photonics Res. **4**, 257 (2016).
[31] P. Colman, C. W. Wong, S. Combrié, A. De Rossi, and C. Husko, Effect of multiphoton absorption and free carriers in slow-light photonic crystal waveguides, Opt. Lett. **36**, 2239 (2011).
[32] A. Blanco-Redondo, C. Husko, D. Eades, Y. Zhang, J. Li, T. F. Krauss, and B. J. Eggleton, Observation of soliton compression in silicon photonic crystals, Nat. Commun. **5**, 3160 (2014).
[33] T. Kampfrath, D. M. Beggs, T. P. White, A. Melloni, T. F. Krauss, and L. Kuipers, Ultrafast adiabatic manipulation of slow light in a photonic crystal, Phys. Rev. A **81**, 043837 (2010).
[34] J. Upham, Y. Tanaka, T. Asano, and S. Noda, On-the-fly wavelength conversion of photons by dynamic control of photonic waveguides, Appl. Phys. Express **3**, 062001 (2010).
[35] J. Upham, H. Inoue, Y. Tanaka, W. Stumpf, K. Kojima, T. Asano, and S. Noda, Pulse capture without carrier absorption in dynamic Q photonic crystal nanocavities, Opt. Express **22**, 15459 (2014).
[36] M. A. Gaafar, H. Li, X. Cai, J. Li, M. Eich, and A. Y. Petrov, Optical push broom on a chip, arXiv:2010.12424.
[37] E. Lustig *et al.*, Time-refraction optics with single cycle modulation, Nanophotonics **12**, 2221 (2023).
[38] J. Bohn, T. S. Luk, T. S. Luk, S. Horsley, and E. Hendry, Spatiotemporal refraction of light in an epsilon-near-zero indium tin oxide layer: Frequency shifting effects arising from interfaces, Opt. **8**, 1532 (2021).
[39] Q. Lin *et al.*, Nonlinear optical phenomena in silicon waveguides: Modeling and applications, Opt. Express **15**, 16604 (2007).
[40] S. A. Schulz, L. O'Faolain, D. M. Beggs, T. P. White, A. Melloni, and T. F. Krauss, Dispersion engineered slow light in photonic crystals: A comparison, J. Opt. **12**, 104004 (2010).
[41] M. Verbist, W. Bogaerts, and D. Van Thourhout, Design of weak 1-D Bragg grating filters in SOI waveguides using volume holography techniques, J. Light. Technol. **32**, 1915 (2014).
[42] M. Verbist, D. Van Thourhout, and W. Bogaerts, Weak gratings in silicon-on-insulator for spectral filters based on volume holography, Opt. Lett. **38**, 386 (2013).
[43] M. Lobet, N. Kinsey, I. Liberal, H. Caglayan, P. A. Huidobro, E. Galiffi, J. R. Mejía-Salazar, G. Palermo, Z. Jacob, and N. Maccaferri, New horizons in near-zero refractive index photonics and hyperbolic metamaterials, ACS Photonics **10**, 3805 (2023).
[44] Y. Ding, H. Ou, and C. Peucheret, Ultrahigh-efficiency apodized grating coupler using fully etched photonic crystals, Opt. Lett. **38**, 2732 (2013).
[45] M. A. Gaafar, H. Renner, A. Y. Petrov, and M. Eich, Linear Schrödinger equation with temporal evolution for front induced transitions, Opt. Express **27**, 21273 (2019).
[46] C. M. de Sterke and J. E. Sipe, Envelope-function approach for the electrodynamics of nonlinear periodic structures, Phys. Rev. A **38**, 5149 (1988).
[47] N. A. R. Bhat and J. E. Sipe, Optical pulse propagation in nonlinear photonic crystals, Phys. Rev. E **64**, 056604 (2001).

[48] J. A. C. Weideman and B. M. Herbst, Split-step methods for the solution of the nonlinear Schrödinger equation, SIAM J. Numer. Anal. **23**, 485 (1986).

[49] E. J. Reed, M. Soljačić, and J. D. Joannopoulos, Reversed Doppler effect in photonic crystals, Phys. Rev. Lett. **91**, 133901 (2003).

[50] R. Dekker, A. Driessen, T. Wahlbrink, C. Moormann, J. Niehusmann, and M. Först, Ultrafast Kerr-induced all-optical wavelength conversion in silicon waveguides using 1.55 μm femtosecond pulses, Opt. Express **14**, 8336 (2006).

[51] Y. Ding, C. Peucheret, H. Ou, and K. Yvind, Fully etched apodized grating coupler on the SOI platform with −0.58 dB coupling efficiency, Opt. Lett. **39**, 5348 (2014).

[52] R. Soref and B. Bennett, Electrooptical effects in silicon, IEEE J. Quantum Electron. **23**, 123 (1987).